crystals

MDPI

Article

Ginzburg–Landau Analysis on the Physical Properties of the Kagome Superconductor CsV_3Sb_5

Tianyi Han [1], Jiantao Che [1], Chenxiao Ye [2] and Hai Huang [1,*]

[1] Department of Mathematics and Physics, North China Electric Power University, Beijing 102206, China
[2] School of Nuclear Science and Engineering, North China Electric Power University, Beijing 102206, China
* Correspondence: huanghai@ncepu.edu.cn

Abstract: The kagome lattice consisting of corner-sharing triangles has been studied in the context of quantum physics for more than seventy years. For the novel discovered kagome superconductor CsV_3Sb_5, identifying the pairing symmetry of order parameter remained an elusive problem until now. Based on the two-band Ginzburg–Landau theory, we study the temperature dependence of upper critical field and magnetic penetration depth for this compound. All theoretical results are consistent with the experimental data, which strongly indicates the existence of two-gap *s*-wave superconductivity in this system. In addition, it is worth noting that the anisotropy of effective masses in the band with large (or small) gap is about 70 (or 2.4). With the calculation of the Kadowaki–Woods ratio as 0.58×10^{-5} μΩ cm mol^2 K^2 mJ^{-2}, the semi-heavy-fermion feature is suggested in the compound CsV_3Sb_5.

Keywords: Ginzburg–Landau theory; two-gap *s*-wave superconductivity; CsV_3Sb_5; heavy fermion system

check for updates

Citation: Han, T.; Che, J.; Ye, C.; Huang, H. Ginzburg–Landau Analysis on the Physical Properties of the Kagome Superconductor CsV_3Sb_5. *Crystals* **2023**, *13*, 321. https://doi.org/10.3390/cryst13020321

Academic Editor: Jacek Ćwik

Received: 21 January 2023
Revised: 10 February 2023
Accepted: 12 February 2023
Published: 15 February 2023

Copyright: © 2023 by the authors. Licensee MDPI, Basel, Switzerland. This article is an open access article distributed under the terms and conditions of the Creative Commons Attribution (CC BY) license (https://creativecommons.org/licenses/by/4.0/).

1. Introduction

The recently discovered kagome metal series AV_3Sb_5 (A = K, Rb, Cs) exhibit topologically nontrivial band structures, chiral charge order, charge density wave (CDW) and superconductivity, presenting a unique platform for realizing exotic electronic states [1–6]. These materials crystallize in the $P6/mmm$ space group with ideal kagome nets of V atoms which are coordinated by Sb atoms. The kagome layers of CsV_3Sb_5 are sandwiched by extra antimonene layers and Cs layers, as shown in the inset of Figure 1. With the decrease in temperature, the CDW phase transition takes place at about 94 K for CsV_3Sb_5 [7–11]. Based on the density functional theory, the first principle calculations show that the CDW observed in this family of compounds is a consequence of the atomic displacement from the high-symmetry positions of the kagome network [12,13]. Meanwhile, the experimental measurements with Raman spectroscopy have also confirmed the dynamical lattice distortions in the CDW phase [14–16]. Then, below about 2.5 K superconductivity is observed and coexists with the CDW order without further structural transitions [17–23].

For a series of hexagonal symmetric layered materials, the electronic band structure and topological properties have already been carried out based on the numerical ab initio calculations [24,25]. Furthermore, it is also well known that the two-dimensional kagome lattice hosts a pair of Dirac bands protected from the lattice symmetry and will trigger the correlated topological states of matter. For the three-dimensional crystal CsV_3Sb_5, V 3*d* and Sb 5*p* orbitals play dominant contributions to the density of states near the Fermi level, and the nontrivial band crossing is extended along a one-dimensional line in the Brillouin zone. Such band structure features are associated with a $\mathbb{Z}_2$ topological index [2,26], and the topological surface states can be easily observed if a direct gap exists for every momentum in this system. Additionally, electronic transport and heat capacity measurements reveal a large Kadowaki–Woods (KW) ratio. It indicates the V-based kagome prototype structure may be of potential interest as a host of correlated electron phenomenon, particularly as a heavy-fermion material.

Up to now, several theoretical and experimental investigations have already been performed on the pairing symmetry of the kagome compound CsV_3Sb_5. Multiband structure of this compound was predicted by previous theoretical calculations and then confirmed by angle-resolved photoemission spectroscopy studies [27–31]. Meanwhile, the measurement of nuclear magnetic resonance on this kagome metal showed a Hebel–Slichter coherence peak just below T_c, indicating that CsV_3Sb_5 is an *s*-wave superconductor [11]. Magnetic penetration depth of this system measured by tunneling diode oscillator displayed a clear exponential behavior at low temperatures, which also provides evidence for the nodeless structure in this compound. Furthermore, experimental data on temperature dependence of the superfluid density and electronic specific heat can be well described by two-gap superconductivity scenario [32], which is consistent with the presence of multiple Fermi surfaces in this system. Obviously, to date there is still no general consensus on the form of superconducting order parameter in CsV_3Sb_5 and further explorations to elucidate this issue are necessary.

The main motivation of the present paper is to identify the form of order parameter in this kagome superconductor. Based on the two-band Ginzburg–Landau (GL) theory, we study the temperature dependence of upper critical field and magnetic penetration depth for this compound. Our results can fit the experimental data well in a broad temperature range, which thus strongly suggests CsV_3Sb_5 as a two-gap *s*-wave superconductor. We can also obtain the effective mass of the electron in the *c*-axis for the first band as $38m_e$ and only $0.31m_e$ for the other band. With this semi-heavy-fermion feature, we can qualitatively understand the experimental value of the KW ratio in CsV_3Sb_5.

The paper is organized as follows: In the next section, we discuss the two-band GL theory. We derive the formula for the critical temperature and discuss how to properly choose the parameters in the GL theory. In Section 3, we calculate the upper critical field H_{c2} for the kagome superconductor CsV_3Sb_5. Then in Section 4, we work out the magnetic penetration depth for this compound. In Section 5, we discuss the KW ratio and semi-heavy-fermion feature in this material. Finally, Section 6 contains the conclusion of the paper.

2. Two-Band Anisotropic Ginzburg–Landau Theory

Taking into account the multi-gap characteristics of V-based superconductors, we can note the two-band GL free energy functional as [33–35].

$$F = \int d^3\mathbf{r}(f_1 + f_2 + f_{12} + \mathbf{H}^2/8\pi), \tag{1}$$

with

$$\begin{aligned} f_i = &\frac{\hbar^2}{2m_i}\left|\left(\partial_x - \frac{2ieA_x}{\hbar c}\right)\Psi_i\right|^2 + \frac{\hbar^2}{2m_i}\left|\left(\partial_y - \frac{2ieA_y}{\hbar c}\right)\Psi_i\right|^2 + \frac{\hbar^2}{2m_{iz}}\left|\left(\partial_z - \frac{2ieA_z}{\hbar c}\right)\Psi_i\right|^2 \\ &- \alpha_i(T)|\Psi_i|^2 + \frac{\beta_i}{2}|\Psi_i|^4 \end{aligned} \tag{2}$$

and

$$f_{12} = \eta_{12}(\Psi_1^*\Psi_2 + \text{c.c.}). \tag{3}$$

Here, f_i $(i = 1, 2)$ is the free energy density for each band and f_{12} is the interaction-free energy density. $\Psi_i \propto \sqrt{N_i}\Delta_i$ with N_i the density of states at the Fermi level is the superconducting order parameter and $N_1/N_2 = 0.79/0.21$ from the specific heat data in CsV_3Sb_5 [32]. m_i and m_{iz} denote the effective masses in the *ab*-plane and in the *c*-direction for band *i*. From the measurement of Shubnikov–de Haas oscillations with the magnetic field parallel to the *c*-direction, we have $m_1 = 0.55m_e$ and $m_2 = 0.13m_e$ [36]. η_{12} is the Josephson coupling constant. The coefficient α_i is a function of temperature, while β_i is independent of temperature. If the interband interaction is neglected, the functional can be reduced to two independent single-band problems with the corresponding critical temperatures T_{c1} and T_{c2}, respectively. Thus, the parameters α_1 and α_2 can be approximately

expressed as $\alpha_i = \alpha_{i0}(1 - T/T_{ci})$ with α_{i0} the proportionality constant [37]. $\mathbf{H} = \nabla \times \mathbf{A}$ is magnetic field and $\mathbf{A} = (A_x, A_y, A_z)$ is the vector potential.

By minimizing the free energy F with Ψ_i^*, we can obtain the GL equations for the description of the two-band superconductivity

$$\hat{M}_{11}\Psi_1 + \hat{M}_{12}\Psi_2 = 0 \tag{4}$$

and

$$\hat{M}_{21}\Psi_1 + \hat{M}_{22}\Psi_2 = 0, \tag{5}$$

with

$$\begin{aligned}\hat{M}_{ii} = &-\frac{\hbar^2}{2m_i}\left(\partial_x - \frac{2ieA_x}{\hbar c}\right)^2 - \frac{\hbar^2}{2m_i}\left(\partial_y - \frac{2ieA_y}{\hbar c}\right)^2 - \frac{\hbar^2}{2m_{iz}}\left(\partial_z - \frac{2ieA_z}{\hbar c}\right)^2 \\ &- \alpha_i + \beta_i|\Psi_i|^2\end{aligned} \tag{6}$$

and

$$\hat{M}_{12} = \hat{M}_{21} = \eta_{12}. \tag{7}$$

By minimizing the free energy F with the vector potential $\mathbf{A}$, we then obtain the equation for the current $\mathbf{j} = (j_x, j_y, j_z)$ as

$$\nabla \times \mathbf{H} = 4\pi\mathbf{j} \tag{8}$$

with

$$j_x = \frac{e}{ic}\sum_i\left(\frac{\hbar}{m_i}\Psi_i^*\partial_x\Psi_i - \frac{\hbar}{m_i}\Psi_i\partial_x\Psi_i^* - \frac{4ie}{m_i c}\Psi_i^*\Psi_i A_x\right), \tag{9}$$

$$j_y = \frac{e}{ic}\sum_i\left(\frac{\hbar}{m_i}\Psi_i^*\partial_y\Psi_i - \frac{\hbar}{m_i}\Psi_i\partial_y\Psi_i^* - \frac{4ie}{m_i c}\Psi_i^*\Psi_i A_y\right) \tag{10}$$

and

$$j_z = \frac{e}{ic}\sum_i\left(\frac{\hbar}{m_{iz}}\Psi_i^*\partial_z\Psi_i - \frac{\hbar}{m_{iz}}\Psi_i\partial_z\Psi_i^* - \frac{4ie}{m_{iz}c}\Psi_i^*\Psi_i A_z\right). \tag{11}$$

Equations (4), (5) and (8) are the fundamental GL equations for the two-gap superconductors. In the absence of fields and gradients, Equations (4) and (5) give

$$\left(-\alpha_1 + \beta_1|\Psi_1|^2\right)\Psi_1 + \eta_{12}\Psi_2 = 0 \tag{12}$$

and

$$\eta_{12}\Psi_1 + \left(-\alpha_2 + \beta_2|\Psi_2|^2\right)\Psi_2 = 0. \tag{13}$$

At $T \to T_c$, we get

$$\alpha_1(T_c)\alpha_2(T_c) = \eta_{12}^2. \tag{14}$$

With $T_c = 2.5$ K for CsV_3Sb_5, we can easily get η_{12} from the equation above.

In principle, we can derive the parameters in our GL theory from microscopic two-band BCS theory. Following Ref. [35], if we compare the microscopic forms of α_i and β_i, we can obtain two useful relations $\alpha_{10}/\alpha_{20} = T_{c1}/T_{c2}$ and $\beta_1 = \beta_2$. Since two superconducting gaps appear at $1.6k_BT_c$ and $0.63k_BT_c$ [32], we can approximate T_{c1}/T_{c2} as $1.6/0.63 \approx 2.5$. In addition, it has been proven that the ratio of energy gaps at zero temperature is equal to that at critical temperature [38], and according to Equations (12)–(14) the ratio of energy gaps at T_c can be written as $|(\Psi_1/\sqrt{N_1})/(\Psi_2/\sqrt{N_2})| = \sqrt{(N_2/N_1)[\alpha_2(T_c)/\alpha_1(T_c)]}$. Then with simple algebra, we can obtain $T_{c1} = 2.4$ K from this condition.

3. Calculation on the Upper Critical Field of CsV_3Sb_5

3.1. The Upper Critical Field Parallel to the c-Axis

Now let us solve the problem of the nucleation of superconductivity in the presence of a field **H**. With the magnetic field along the *c*-axis, the vector potential **A** can be chosen as **A** = (0, Hx, 0). Since the vector potential depends only on x, similar to the single-band case, we can look for solution with the form

$$\Psi_i = e^{ik_y y} e^{ik_z z} f_i(x). \tag{15}$$

Near the upper critical field, the quartic terms in Equation (2) can be ignored, so the linearized two-band GL equations take the form

$$\hat{M}_{11} f_1(x) + \hat{M}_{12} f_2(x) = 0 \tag{16}$$

and

$$\hat{M}_{21} f_1(x) + \hat{M}_{22} f_2(x) = 0 \tag{17}$$

with

$$\hat{M}_{ii} = -\frac{\hbar^2}{2m_i}\frac{d^2}{dx^2} + \frac{1}{2}m_i\omega_i^2(x - x_0)^2 - \alpha_i + \frac{\hbar^2}{2m_{iz}}k_z^2. \tag{18}$$

Here $\omega_i = 2eH/m_i c$ and $x_0 = \hbar c k_y / 2eH$. Thus, inclusion of the factor $e^{ik_y y}$ only shifts the location of the minimum of the effective potential. This is unimportant for the present, but it will become important when we deal with superconductivity near surfaces of finite samples [39,40]. We can also set $k_z = 0$ if we only consider the upper critical field [39].

At $\eta_{12} = 0$, we can obtain the solutions to Equations (16) and (17) immediately by noting that, for each band, it is the Schrödinger equation for a particle bound in a harmonic oscillator potential. The resulting harmonic oscillator eigenvalues are

$$E_{i,n} = (n + 1/2)\hbar\omega_i - \alpha_i. \qquad (n = 0, 1, 2, \ldots) \tag{19}$$

If $\eta_{12} \neq 0$, Equations (16) and (17) describe a system of two coupled oscillators. We can set the form of the solutions as

$$f_1(x) = c_1 \left(\frac{b}{\pi}\right)^{1/4} e^{-bx^2/2} \tag{20}$$

and

$$f_2(x) = c_2 \left(\frac{b}{\pi}\right)^{1/4} e^{-bx^2/2}. \tag{21}$$

Here c_1, c_2 are constants, and $b = 2\pi H/\Phi_0$ with the magnetic flux quantum $\Phi_0 = \pi\hbar c/e$. Thus, for $n = 0$, we can transform Equations (16) and (17) into

$$E_{1,0} c_1 + \eta_{12} c_2 = \varepsilon c_1 = 0 \tag{22}$$

and

$$\eta_{12} c_1 + E_{2,0} c_2 = \varepsilon c_2 = 0. \tag{23}$$

with ε the eigenvalue of the matrix.

Then we can obtain the upper critical field parallel to the *c*-axis from the minimum energy eigenvalue

$$\varepsilon_{min} = \frac{1}{2}\left[(E_{1,0} + E_{2,0}) - \sqrt{(E_{1,0} - E_{2,0})^2 + 4\eta_{12}^2}\right] = 0, \tag{24}$$

which can be simplified as

$$E_{1,0} E_{2,0} = \eta_{12}^2. \tag{25}$$

With $E_{i,0} = \hbar\omega_i/2 - \alpha_i$ and $\omega_i = 2eH_{c2}^{\|c}/m_i c$, we get from Equation (25)

$$\left(\frac{\hbar e}{m_1 c}H_{c2}^{\|c} - \alpha_1\right)\left(\frac{\hbar e}{m_2 c}H_{c2}^{\|c} - \alpha_2\right) = \eta_{12}^2. \tag{26}$$

Simple algebra shows that the upper critical field can be expressed as

$$H_{c2}^{\|c} = \frac{\Phi_0}{2\pi\hbar^2}\left[(m_1\alpha_1 + m_2\alpha_2) + \sqrt{(m_1\alpha_1 - m_2\alpha_2)^2 + 4m_1m_2\eta_{12}^2}\right]. \tag{27}$$

Single crystals of CsV_3Sb_5 can be synthesized via a self-flux growth method [41–43]. In order to prevent the reaction of Cs with air and water, all the preparation processes are performed in an argon glovebox. After high temperature reaction in the furnace, the excess flux is removed by water and a millimeter-sized single crystal can be obtained. The as-grown CsV_3Sb_5 single crystals are stable in the air. Then electrical transport measurements can be carried out in a Quantum Design physical property measurement system (PPMS-14T), and magnetization measurements can be performed in a SQUID magnetometer (MPMS-5T). For CsV_3Sb_5, the experimental data of the upper critical field can be measured following these steps and then shown in Figure 1.

To fit the experimental measurement, we choose the GL parameter $\alpha_{10} = 0.11$ meV. According to Equation (27), we plot the theoretical result of $H_{c2}^{\|c}$ as the solid line in Figure 1. Note that the experimental data are almost linear and our calculation fits the experimental measurement well.

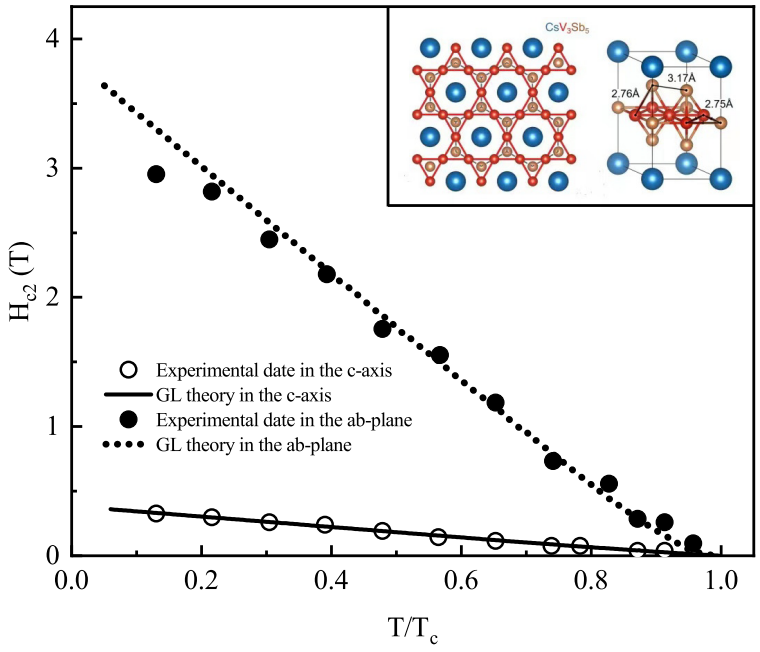


Figure 1. Upper critical field $H_{c2}^{\|c}$ (solid line) and $H_{c2}^{\|ab}$ (dotted line) as function of temperature. The experimental data are from Ref. [43]. The inset shows the schematic crystal structure of CsV_3Sb_5.

3.2. The Upper Critical Field Parallel to the ab-Plane

In this subsection, we will study the nucleation of superconductivity with the magnetic field **H** applied in the *ab*-plane. We set $\mathbf{H} = (0, H, 0)$ and take $\mathbf{A} = (0, 0, -Hx)$. Similarly, we look for a solution with the form (15). Close to the upper critical field we can also obtain the linearized GL Equations (16) and (17), but the diagonal element of the $\hat{M}$-matrix changes into

$$\hat{M}_{ii} = -\frac{\hbar^2}{2m_i}\frac{d^2}{dx^2} + \frac{1}{2}m_i\omega_i'^2\left(x + x_0'\right)^2 - \alpha_i, \tag{28}$$

where $\omega_i' = 2eH/c\sqrt{m_i m_{iz}}$ and $x_0' = \hbar c k_z/2eH$.

If $\eta_{12} = 0$, analogous to the analysis of the last subsection, the harmonic oscillator eigenvalues are

$$E_{i,n}' = (n + 1/2)\hbar\omega_i' - \alpha_i. \qquad (n = 0, 1, 2, \ldots) \tag{29}$$

If $\eta_{12} \neq 0$, we cannot get an exact result due to the mixing between the minimum and higher-level eigenfunctions. We thus follow a variational approach. We look for a solution in the form

$$f_1(x) = c_1 g_1(x) = c_1 \left(\frac{b_1}{\pi}\right)^{1/4} e^{-b_1 x^2/2} \tag{30}$$

and

$$f_2(x) = c_2 g_2(x) = c_2 \left(\frac{b_2}{\pi}\right)^{1/4} e^{-b_2 x^2/2}, \tag{31}$$

with b_1 and b_2 the variational parameters. Introducing $D_{ij} = \langle g_i | \hat{M}_{ij} | g_j \rangle$, detailed calculations give

$$D_{11} = \frac{\hbar^2 b_1}{4m_1} + \frac{e^2 H^2}{m_{1z} c^2 b_1} - \alpha_1, \tag{32}$$

$$D_{22} = \frac{\hbar^2 b_2}{4m_2} + \frac{e^2 H^2}{m_{2z} c^2 b_2} - \alpha_2 \tag{33}$$

and

$$D_{12} = D_{21} = \eta_{12} (b_1 b_2)^{1/4} \left(\frac{2}{b_1 + b_2}\right)^{1/2}. \tag{34}$$

Then we can transform Equations (16), (17) and (28) into

$$D_{11} c_1 + D_{12} c_2 = \varepsilon' c_1 = 0 \tag{35}$$

and

$$D_{21} c_1 + D_{22} c_2 = \varepsilon' c_2 = 0. \tag{36}$$

Let ε' denote the eigenvalue of the D-matrix. The upper critical field corresponds to the minimum eigenvalue $\varepsilon'_{min} = 0$, and it is available from Equations (35) and (36) as

$$\varepsilon'_{min} = \frac{1}{2}\left[(D_{11} + D_{22}) - \sqrt{(D_{11} - D_{22})^2 + 4D_{12}D_{21}}\right]. \tag{37}$$

Minimizing ε'_{min} with respect to b_1 and b_2

$$\frac{\partial \varepsilon'_{min}}{\partial b_1} = 0 \qquad \text{and} \qquad \frac{\partial \varepsilon'_{min}}{\partial b_2} = 0, \tag{38}$$

and combining with

$$\varepsilon'_{min}\left(H_{c2}^{\|ab}, b_1, b_2\right) = 0, \tag{39}$$

we can obtain the upper critical field $H_{c2}^{\|ab}$ at an arbitrary temperature.

We choose the GL parameters $m_{1z} = 38m_e$ and $m_{2z} = 0.31m_e$ to fit the experimental data. By numerically solving three nonlinear Equations (38) and (39), we plot the theoretical result of $H_{c2}^{\|ab}$ as the dotted line in Figure 1. Note that our calculation is in agreement with the experimental measurement of $H_{c2}^{\|ab}$ in temperature down to $0.2T_c$.

4. Calculation on the Magnetic Penetration Depth of CsV_3Sb_5

Now we begin to calculate the magnetic penetration depth for this two-band superconductor. In the presence of the weak fields, the solution takes the form [39]

$$\Psi_i(\mathbf{r}) = |\Psi_i| e^{i\varphi_i(\mathbf{r})}, \tag{40}$$

where $|\Psi_i|$ is constant. If the external field is applied parallel to the c-axis, we can set $\mathbf{A} = (A_x, A_y, 0)$, and without loss of generality we consider the phase factor φ_i as a function of x and y. From Equation (8), we get

$$\frac{\nabla \times \mathbf{H}}{4\pi} = \frac{2e\hbar}{m_1 c}|\Psi_1|^2\left(\nabla\varphi_1 - \frac{2e}{\hbar c}\mathbf{A}\right) + \frac{2e\hbar}{m_2 c}|\Psi_2|^2\left(\nabla\varphi_2 - \frac{2e}{\hbar c}\mathbf{A}\right). \tag{41}$$

Then following the standard procedure in Ref. [39], we can rewrite Equation (41) as

$$\nabla^2\mathbf{H} - \left(\frac{16\pi e^2}{m_1 c^2}|\Psi_1|^2 + \frac{16\pi e^2}{m_2 c^2}|\Psi_2|^2\right)\mathbf{H} = 0. \tag{42}$$

Therefore, we can obtain the magnetic penetration depth in the ab-plane as

$$\lambda_{ab} = \left(\frac{m_1 m_2 c^2}{16\pi m_2 e^2|\Psi_1|^2 + 16\pi m_1 e^2|\Psi_2|^2}\right)^{1/2}. \tag{43}$$

Similarly, the magnetic penetration depth along the c-axis is given by

$$\lambda_c = \left(\frac{m_{1z} m_{2z} c^2}{16\pi m_{2z} e^2|\Psi_1|^2 + 16\pi m_{1z} e^2|\Psi_2|^2}\right)^{1/2}. \tag{44}$$

We take $\beta_1 = 1.3 \times 10^{-2}$ meV·μm^3 to fit the experimental data on the magnetic penetration depth. First of all, $|\Psi_1|$ and $|\Psi_2|$ as function of temperature can be numerically obtained from Equations (12) and (13). Then from Equations (43) and (44), we plot λ_{ab} and λ_c as function of temperature in Figure 2. From Figure 2, we can see that our theoretical calculation can fit the experimental data well almost in the whole temperature range.

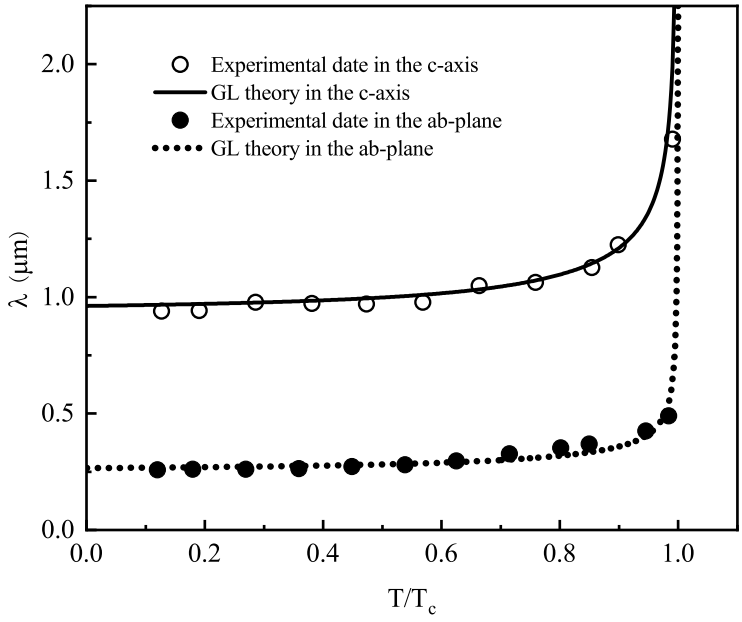


Figure 2. Magnetic penetration depth along the c-axis (solid line) and in the ab-plane (dotted line) as function of temperature. The experimental data are from Ref. [43].

At this stage, we would also like to point out that Gupta et al. also tried to fit the experimental data of the magnetic penetration depth with the *d*-wave model [43]. However, compared with the two-gap *s*-wave model, the *d*-wave model does not describe the data well, which provides further evidence for the nodeless structure in this compound.

5. KW Ratio and the Semi-Heavy–Fermion System

In this section, we would like to discuss the KW ratio and semi-heavy-fermion feature in the compound CsV_3Sb_5. Since the discovery by Steglich et al. of superconductivity in the high-effective-mass ($\sim 100m_e$) electrons in $CeCu_2Si_2$, the search for and characterization of such heavy-fermion systems has been a rapidly growing field of study [44]. In a Fermi liquid, the electronic contribution to the heat capacity has a linear temperature dependence $C_{el}(T) = \gamma T$, and at low temperatures the resistivity varies as $\rho(T) = \rho_0 + AT^2$. This is observed experimentally when electron–electron scattering, which gives rise to the quadratic term, dominates over electron–phonon scattering in the process. In a number of typical transition metals, we have $A/\gamma^2 \approx 0.09 \times 10^{-5}$ μΩ cm mol^2 K^2 mJ^{-2} even though γ^2 varies by an order of magnitude across the materials studied. Meanwhile, it was found in many heavy-fermion compounds A/γ^2 reaches 1.0×10^{-5} μΩ cm mol^2 K^2 mJ^{-2} despite the large mass renormalization. Because of this remarkable behavior A/γ^2 has become known as the KW ratio, and large value of this ratio is treated as a robust signature of heavy-fermion systems [45,46].

With the effective masses in the *ab*-plane ($m_1 = 0.55m_e$, $m_2 = 0.13m_e$) [36] and those along the *c*-direction ($m_{1z} = 38m_e$, $m_{2z} = 0.31m_e$) from the two-band GL theory, we can expect that the first band in CsV_3Sb_5 will show the heavy-fermion properties, while the other band can be treated as the normal metal. Meanwhile, for this kagome crystal we have resistivity coefficient $A = 2.3 \times 10^{-3}$ μΩ cm K^{-2} from the electronic transport measurement and Sommerfeld factor $\gamma = 20$ mJ mol^{-1} K^{-2} from the specific heat data [32]. It is thus reasonable that CsV_3Sb_5, as a semi-heavy-fermion compound, possesses a medium KW ratio $A/\gamma^2 \approx 0.58 \times 10^{-5}$ μΩ cm mol^2 K^2 mJ^{-2} between 0.09×10^{-5} and 1.0×10^{-5} μΩ cm mol^2 K^2 mJ^{-2}.

6. Conclusions

In summary, based on the two-band anisotropic GL theory, we studied the temperature dependence of upper critical field and magnetic penetration depth for the kagome superconductor CsV_3Sb_5. Our theoretical results fit the experimental data in a broad temperature range, pointing to the existence of two-gap *s*-wave superconductivity in this system. From the large anisotropy of effective masses in the first band, we also suggest that CsV_3Sb_5 is a semi-heavy-fermion compound. The possible mechanism of the semi-heavy-fermion state and other problems for these kinds of materials are reserved for further investigations.

Author Contributions: Conceptualization, T.H., J.C., C.Y. and H.H.; methodology, T.H., J.C., C.Y. and H.H.; software, T.H.; validation, T.H., J.C., C.Y. and H.H.; formal analysis, T.H., J.C., C.Y. and H.H.; investigation, T.H., J.C., C.Y. and H.H.; resources, H.H.; data curation, T.H., J.C., C.Y. and H.H.; writing—original draft preparation, T.H.; writing—review and editing, T.H., J.C., C.Y. and H.H.; visualization, T.H.; supervision, J.C., C.Y. and H.H.; project administration, H.H. All authors have read and agreed to the published version of the manuscript.

Funding: This research received no external funding.

Data Availability Statement: Not applicable.

Conflicts of Interest: The authors declare no conflict of interest.

References

1. Ortiz, B.R.; Gomes, L.C.; Morey, J.R.; Winiarski, M.; Oswald, I.W.H.; Mangum, J.S.; Neilson, J.R.; Ertekin, E.; McQueen, T.M.; Toberer, E.S. New kagome prototype materials: Discovery of KV_3Sb_5, RbV_3Sb_5 and CsV_3Sb_5. *Phys. Rev. Mater.* **2019**, *3*, 094407. [CrossRef]
2. Ortiz, B.R.; Teicher, S.M.L.; Hu, Y.; Zuo, J.L.; Sarte, P.M.; Schueller, E.C.; Abeykoon, A.M.M.; Krogstad, M.J.; Rosenkranz, S.; Osborn, R.; et al. CsV_3Sb_5: A $\mathbb{Z}_2$ topological kagome metal with a superconducting ground state. *Phys. Rev. Lett.* **2020**, *125*, 247002. [CrossRef] [PubMed]
3. Ortiz, B.R.; Sarte, P.M.; Kenney, E.M.; Graf, M.J.; Teicher, S.M.L.; Seshadri, R.; Wilson, S.D. Superconductivity in the $\mathbb{Z}_2$ kagome metal KV_3Sb_5. *Phys. Rev. Mater.* **2021**, *5*, 034801. [CrossRef]
4. Yin, Q.W.; Tu, Z.J.; Gong, C.S.; Fu, Y.; Yan, S.H.; Lei, H.C. Superconductivity and normal-state properties of kagome metal RbV_3Sb_5 single crystals. *Chin. Phys. Lett.* **2021**, *38*, 037403. [CrossRef]
5. Shumiya, N.; Hossain, M.S.; Yin, J.X.; Jiang, Y.X.; Ortiz, B.R.; Liu, H.X.; Shi, Y.G.; Yin, Q.W.; Lei, H.C.; Zhang, S.T.S.; et al. Intrinsic nature of chiral charge order in the kagome superconductor RbV_3Sb_5. *Phys. Rev. B* **2021**, *104*, 035131. [CrossRef]
6. Guguchia, Z.; Mielke, C., III; Das, D.; Gupta, R.; Yin, J.X.; Liu, H.; Yin, Q.; Christensen, M.H.; Tu, Z.; Gong, C.; et al. Tunable unconventional kagome superconductivity in charge ordered RbV_3Sb_5 and KV_3Sb_5. *Nat. Commun.* **2023**, *14*, 153. [CrossRef]
7. Li, H.X.; Zhang, T.T.; Yilmaz, T.; Pai, Y.Y.; Marvinney, C.E.; Said, A.; Yin, Q.W.; Gong, C.S.; Tu, Z.J.; Vescovo, E.; et al. Observation of unconventional charge density wave without acoustic phonon anomaly in kagome superconductors AV_3Sb_5(A = Rb, Cs). *Phys. Rev. X* **2021**, *11*, 031050. [CrossRef]
8. Liang, Z.W.; Hou, X.Y.; Zhang, F.; Ma, W.R.; Wu, P.; Zhang, Z.Y.; Yu, F.H.; Ying, J.J.; Jiang, K.; Shan, L.; et al. Three-dimensional charge density wave and surface-dependent vortex-core states in a kagome superconductor CsV_3Sb_5. *Phys. Rev. X* **2021**, *11*, 031026. [CrossRef]
9. Zhao, H.; Li, H.; Ortiz, B.R.; Teicher, S.M.L.; Park, T.; Ye, M.X.; Wang, Z.Q.; Balents, L.; Wilson, S.D.; Zeljkovic, I. Cascade of correlated electron states in the kagome superconductor CsV_3Sb_5. *Nature* **2021**, *599*, 216. [CrossRef]
10. Ortiz, B.R.; Teicher, S.M.L.; Kautzsch, L.; Sarte, P.M.; Ratcliff, N.; Harter, J.; Ruff, J.P.C.; Seshadri, R.; Wilson, S.D. Fermi surface mapping and the nature of charge-density-wave order in the kagome superconductor CsV_3Sb_5. *Phys. Rev. X* **2021**, *11*, 041030. [CrossRef]
11. Mu, C.; Yin, Q.W.; Tu, Z.J.; Gong, C.S.; Lei, H.C.; Li, Z.; Luo, J.L. *S*-wave superconductivity in kagome metal CsV_3Sb_5 revealed by $^{121/123}$Sb NQR and ^{51}V NMR measurements. *Chin. Phys. Lett.* **2021**, *38*, 077402. [CrossRef]
12. Ptok, A.; Kobialka, A.; Sternik, M.; Lazewski, J.; Jochym, P.T.; Oles, M.A.; Piekarz, P. Dynamical study of the origin of the charge density wave in AV_3Sb_5 (A = K, Rb, Cs) compounds. *Phys. Rev. B* **2022**, *105*, 235134. [CrossRef]
13. Subedi, A. Hexagonal-to-base-centered-orthorhombic 4Q charge density wave order in kagome metals KV_3Sb_5, RbV_3Sb_5, and CsV_3Sb_5. *Phys. Rev. Mater.* **2022**, *6*, 015001. [CrossRef]
14. Wang, Z.X.; Wu, Q.; Yin, Q.W.; Gong, C.S.; Tu, Z.J.; Lin, T.; Liu, Q.M.; Shi, L.Y.; Zhang, S.J.; Wu, D.; et al. Unconventional charge density wave and photoinduced lattice symmetry change in the kagome metal CsV_3Sb_5 probed by time-resolved spectroscopy. *Phys. Rev. B* **2021**, *104*, 165110. [CrossRef]
15. Ratcliff, N.; Hallett, L.; Ortiz, B.R.; Wilson, S.D.; Harter, J.W. Coherent phonon spectroscopy and interlayer modulation of charge density wave order in the kagome metal CsV_3Sb_5. *Phys. Rev. Mater.* **2021**, *5*, L111801. [CrossRef]
16. Wulferding, D.; Lee, S.; Choi, Y.; Yin, Q.W.; Tu, Z.J.; Gong, C.S.; Lei, H.C.; Yousuf, S.; Song, J.; Lee, H.; et al. Emergent nematicity and intrinsic versus extrinsic electronic scattering processes in the kagome metal CsV_3Sb_5. *Phys. Rev. Res.* **2022**, *4*, 023215. [CrossRef]
17. Ni, S.L.; Ma, S.; Zhang, Y.H.; Yuan, J.; Yang, H.T.; Lu, Z.Y.W.; Wang, N.N.; Sun, J.P.; Zhao, Z.; Li, D.; et al. Anisotropic superconducting properties of kagome metal CsV_3Sb_5. *Chin. Phys. Lett.* **2021**, *38*, 057403. [CrossRef]
18. Tan, H.X.; Liu, Y.Z.; Wang, Z.Q.; Yan, B.H. Charge density waves and electronic properties of superconducting kagome metals. *Phys. Rev. Lett.* **2021**, *127*, 046401. [CrossRef]
19. Chen, H.; Yang, H.T.; Hu, B.; Zhao, Z.; Yuan, J.; Xing, Y.Q.; Qian, G.J.; Huang, Z.H.; Li, G.; Ye, Y.H.; et al. Roton pair density wave in a strong-coupling kagome superconductor. *Nature* **2021**, *599*, 222. [CrossRef]
20. Jiang, Y.X.; Yin, J.X.; Denner, M.M.; Shumiya, N.; Ortiz, B.R.; Xu, G.; Guguchia, Z.; He, Y.Y.; Hossain, M.S.; Liu, X.X.; et al. Unconventional chiral charge order in kagome superconductor KV_3Sb_5. *Nat. Mater.* **2021**, *20*, 1353. [CrossRef]
21. Du, F.; Luo, S.S.; Ortiz, B.R.; Chen, Y.; Duan, W.Y.; Zhang, D.T.; Lu, X.; Wilson, S.D.; Song, Y.; Yuan, H.Q. Pressure-induced double superconducting domes and charge instability in the kagome metal KV_3Sb_5. *Phys. Rev. B* **2021**, *103*, L220504. [CrossRef]
22. Uykur, E.; Ortiz, B.R.; Wilson, S.D.; Dressel, M.; Tsirlin, A.A. Optical detection of the density-wave instability in the kagome metal KV_3Sb_5. *NPJ Quantum Mater.* **2022**, *7*, 16. [CrossRef]
23. Zhao, C.C.; Wang, L.S.; Xia, W.; Yin, Q.W.; Ni, J.M.; Huang, Y.Y.; Tu, C.P.; Tao, Z.C.; Tu, Z.J.; Gong, C.S.; et al. Nodal superconductivity and superconducting domes in the topological kagome metal CsV_3Sb_5. *arXiv* **2021**, arXiv:abs/2102.08356.
24. Freitas, R.R.Q.; Rivelino, R.; de Brito Mota, F.; de Castilho, C.M.C.; Kakanakova-Georgieva, A.; Gueorguiev, G.K. Topological insulating phases in two-dimensional bismuth-containing single layers preserved by hydrogenation. *J. Phys. Chem. C* **2015**, *119*, 23599. [CrossRef]

25. Freitas, R.R.Q.; de Brito Mota, F.; Rivelino, R.; de Castilho, C.M.C.; Kakanakova-Georgieva, A.; Gueorguiev, G.K. Spin-orbit-induced gap modification in buckled honeycomb XBi and XBi_3 (X = B, Al, Ga, In) sheets. *J. Phys. Condens. Matter* **2015**, *27*, 485306. [CrossRef] [PubMed]
26. Neupert, T.; Denner, M.M.; Yin, J.X.; Thomale, R.; Hasan, M.Z. Charge order and superconductivity in kagome materials. *Nat. Phys.* **2022**, *18*, 137. [CrossRef]
27. Liu, Z.H.; Zhao, N.N.; Yin, Q.W.; Gong, C.S.; Tu, Z.J.; Li, M.; Song, W.H.; Liu, Z.T.; Shen, D.W.; Huang, Y.B.; et al. Charge-density-wave-induced bands renormalization and energy gaps in a kagome superconductor RbV_3Sb_5. *Phys. Rev. X* **2021**, *11*, 041010. [CrossRef]
28. Chen, X.; Zhan, X.H.; Wang, X.J.; Deng, J.; Liu, X.B.; Chen, X.; Guo, J.G.; Chen, X.L. Highly robust reentrant superconductivity in CsV_3Sb_5 under pressure. *Chin. Phys. Lett.* **2021**, *38*, 057402. [CrossRef]
29. Ye, L.D.; Kang, M.G.; Liu, J.W.; Von Cube, F.; Wicker, C.R.; Suzuki, T.; Jozwiak, C.; Bostwick, A.; Rotenberg, E.; Bell, D.C.; et al. Massive Dirac fermions in a ferromagnetic kagome metal. *Nature* **2018**, *555*, 638. [CrossRef]
30. Guo, H.M.; Franz, M. Topological insulator on the kagome lattice. *Phys. Rev. B* **2009**, *80*, 113102. [CrossRef]
31. Mazin, I.I.; Jeschke, H.O.; Lechermann, F.; Lee, H.; Fink, M.; Thomale, R.; Valentí, R. Theoretical prediction of a strongly correlated Dirac metal. *Nat. Commun.* **2014**, *5*, 4261. [CrossRef] [PubMed]
32. Duan, W.Y.; Nie, Z.Y.; Luo, S.S.; Yu, F.H.; Ortiz, B.R.; Yin, L.C.; Su, H.; Du, F.; Wang, A.; Chen, Y.; et al. Nodeless superconductivity in the kagome metal CsV_3Sb_5. *Sci. China Phys. Mech. Astron.* **2021**, *64*, 107462. [CrossRef]
33. Doh, H.; Sigrist, M.; Cho, B.K.; Lee, S.I. Phenomenological theory of superconductivity and magnetism in $Ho_{1-x}Dy_xNi_2B_2C$. *Phys. Rev. Lett.* **1999**, *83*, 5350. [CrossRef]
34. Askerzade, I.N.; Gencer, A.; Güclü, N. On the Ginzburg-Landau analysis of the upper critical field H_{c2} in MgB_2. *Supercond. Sci. Technol.* **2002**, *15*, L13. [CrossRef]
35. Zhitomirsky, M.E.; Dao, V.H. Ginzburg-Landau theory of vortices in a multigap superconductor. *Phys. Rev. B* **2004**, *69*, 054508. [CrossRef]
36. Fu, Y.; Zhao, N.N.; Chen, Z.; Yin, Q.W.; Tu, Z.J.; Gong, C.S.; Xi, C.Y.; Zhu, X.D.; Sun, Y.P.; Liu, K.; et al. Quantum transport evidence of topological band structures of kagome superconductor CsV_3Sb_5. *Phys. Rev. Lett.* **2021**, *12*, 207002. [CrossRef] [PubMed]
37. Kong, Y.; Dolgov, O.V.; Jepsen, O.; Andersen, O.K. Electron-phonon interaction in the normal and superconducting states of MgB_2. *Phys. Rev. B* **2001**, *64*, 020501(R). [CrossRef]
38. Kresin, V.Z. Transport properties and determination of the basic parameters of superconductors with overlapping bands. *J. Low Temp. Phys.* **1973**, *11*, 519. [CrossRef]
39. Tinkham, M. *Introduction to Superconductivity*; McGraw-Hill Inc: New York, NY, USA, 1996.
40. de Gennes, P.G. *Superconductivity of Metals and Alloys*; Westview Press: New York, NY, USA, 1966.
41. Yu, F.H.; Wu, T.; Wang, Z.Y.; Lei, B.; Zhuo, W.Z.; Ying, J.J.; Chen, X.H. Concurrence of anomalous Hall effect and charge density wave in a superconducting topological kagome metal. *Phys. Rev. B* **2021**, *104*, L041103. [CrossRef]
42. Yang, S.Y.; Wang, Y.J.; Ortiz, B.R.; Liu, D.; Gayles, J.; Derunova, E.; Gonzalez-Hernandez, R.; Šmejkal, L.; Chen, Y.L.; Parkin, S.S.P.; et al. Giant, unconventional anomalous Hall effect in the metallic frustrated magnet candidate, KV_3Sb_5. *Sci. Adv.* **2020**, *6*, eabb6003. [CrossRef] [PubMed]
43. Gupta, R.; Das, D.; Mielke, C.H., III; Guguchia, Z.; Shiroka, T.; Baines, C.; Bartkowiak, M.; Luetkens, H.; Khasanov, R.; Yin, Q.; et al. Microscopic evidence for anisotropic multigap superconductivity in the CsV_3Sb_5 kagome superconductor. *NPJ Quantum Mater.* **2022**, *7*, 49. [CrossRef]
44. Steglich, F.; Aarts, J.; Bredl, C.D.; Lieke, W.; Meschede, D.; Franz, W.; Schäfer, H. Superconductivity in the presence of strong pauli paramagnetism: $CeCu_2Si_2$. *Phys. Rev. Lett.* **1979**, *43*, 1892. [CrossRef]
45. Kadowaki, K.; Woods, S.B. Universal relationship of the resistivity and specific heat in heavy-fermion compounds. *Solid State Commun.* **1986**, *58*, 507. [CrossRef]
46. Jacko, A.C.; Fjærestad, J.O.; Powell, B.J. A unified explanation of the Kadowaki-Woods ratio in strongly correlated metals. *Nat. Phys.* **2009**, *5*, 422. [CrossRef]

Disclaimer/Publisher's Note: The statements, opinions and data contained in all publications are solely those of the individual author(s) and contributor(s) and not of MDPI and/or the editor(s). MDPI and/or the editor(s) disclaim responsibility for any injury to people or property resulting from any ideas, methods, instructions or products referred to in the content.